Supplementary Materials for

Inequality embedded in historical anthropogenic $PM_{2.5}$ health impacts

Lulu Chen, Jintai Lin, Randall Martin, Mingxi Du, Hongjian Weng, Hao Kong, Ruijing Ni, Jun Meng, Yuhang Zhang, Lijuan Zhang, Aaron van Donkelaar

Correspondence to: Jintai Lin (linjt@pku.edu.cn; 86-010-62767973)

This PDF file includes:

S1. Explicit GEOS-Chem simulations for selected years

S2. Derivation of consecutive yearly $PM_{2.5}$ concentrations

S2.1 Calculation of consecutive yearly anthropogenic SIOA, BC and POA based on chemical efficiencies

S2.2 Calculation of consecutive yearly anthropogenic SOA

S2.3 Natural and total $PM_{2.5}$

S3. GEOS-Chem evaluation and adjustment

S4. Premature deaths caused by ambient $PM_{2.5}$ exposure

S5. Uncertainty

S6. Decomposition of anthropogenic $PM_{2.5}$-related premature deaths

Supplementary Tables

Table S1. Emissions used in this study.

Table S2. Comparison between simulated and satellite-derived population-weighted surface $PM_{2.5}$ concentrations (μg/m³) from 2000 to 2014.

Supplementary Figures

Fig. S1. Income group classification.

Fig. S2. Method flowchart.

Fig. S3. Annual anthropogenic $PM_{2.5}$-related premature deaths caused by four income groups in 1990.

Fig. S4. Historical changes in annual mean global population-weighted SOA concentrations caused by four groups.

Fig. S5. Historical changes in annual anthropogenic $PM_{2.5}$-related premature deaths.

Fig. S6. Historical annual anthropogenic emissions and population of four groups.

Fig. S7. Spatial distributions of cumulative premature deaths from 1950 to 2014.

Fig. S8. Comparison between our annual mortality results and previous findings.

Fig. S9. Historical changes in global age structure.

Fig. S10. Annual premature deaths attributable to anthropogenic emissions in high-income group.

Fig. S11. Historical changes in anthropogenic $PM_{2.5}$-related premature deaths.

Fig. S12. Historical changes in annual mean global population-weighted $PM_{2.5}$ concentrations caused by anthropogenic emissions in four groups.

Fig. S13. Comparison between $PM_{2.5}$ simulated by the reference $PM_{2.5}$ simulated by GEOS-Chem and the satellite-derived surface $PM_{2.5}$ concentrations ($\mu g/m^3$) in the year of 2014.

Fig. S14. Similar to Fig. S13, but for the year of 2000.

S1. Explicit GEOS-Chem simulations for selected years

We use the global chemical transport model GEOS-Chem version 11-01[1] to estimate the global surface $PM_{2.5}$ concentrations in 1951, 1960, 1970, 1980, 1990, 2000 and 2014. All these years with GEOS-Chem simulations are referred to as simulation years. For each year (e.g., 2014), simulations are run for 18 months, with the first six months used for model spin-up. The basic model setup follows our previous studies[2,3]. Briefly, the model is run with full O_x-NO_x-VOC-CO-HO_x gaseous chemistry and online aerosol calculations. It is driven by the MERRA2 assimilated meteorology at a horizontal resolution of 2.5°longitude × 2.0°latitude with 47 vertical layers with the lowest 10 layers of about 130 m thickness each. Vertical mixing in the planetary boundary layer employs a non-local scheme implemented by Lin et al.[4]. Model convection uses the relaxed Arakawa-Schubert scheme[5]. Dry deposition follows Wesely[6], with a number of modifications[7], for gases and Zhang et al.[8] for aerosols. Wet scavenging of soluble gases and aerosols follows Liu et al.[9], with further updates for BC[10].

Simulated aerosols include SIOA (secondary inorganic aerosol, including sulfate, nitrate and ammonium), black carbon, POA (primary organic aerosol), SOA (secondary organic aerosol), mineral dust and sea salt. The SIOA formation adopts the ISORROPIA II thermodynamic equilibrium model[11], with updates on catalytic heterogeneous sulfate formation following Zhang et al.[12] and Lin et al.[2] and on nitrate formation following Heald et al.[13]. The mass of POA is assumed to be 1.8 times that of primary organic carbon (OC) to account for oxygen atoms contained[14]. The SOA simulation adopts the parameterization by Pye and Seinfeld[15]. Uptake of the hydroperoxyl radical on aerosols follows Lin et al.[16] and Ni et al.[17]. We use the CEDS inventory[18] for global anthropogenic emissions, with those in China over 2000–2014 replaced by MEIC[19-22], which account for the pollution control measures more comprehensively and may better represent the actual emissions in China over the recent years. Other emission information is detailed in Table S1.

We include six full-chemistry simulations in each of those simulation years to estimate the surface $PM_{2.5}$ concentrations contributed by anthropogenic emissions of the four income groups. Contrasting to the control simulation (CTL, i.e. the all-emissions simulation) which contains all anthropogenic and natural emissions, five zero-out simulations exclude anthropogenic emissions globally (xANTH), in the high-income group (xHIGH), in the upper middle group (xUPPER), in

the lower middle group (xLOWER) and in the low-income group (xLOW), respectively. For each component of $PM_{2.5}$, the difference between CTL and xHIGH represents the contribution from anthropogenic emissions in the high-income group; and the contributions from other groups are estimated similarly (denoted by $C^{y}_{g,p,i}$ in Eq. 1). The xANTH simulation (i.e., $C^{y}_{natural,i}$ in Eq. 1) contains the contribution of all $PM_{2.5}$ sources not allocated to the four groups, including natural emissions and international shipping and aviation emissions; hereafter this contribution is referred to as "natural" for simplicity.

As shown in Eq. 1, we use the sum of anthropogenic $PM_{2.5}$ mass concentrations contributed by the four groups and those contributed by all other sources as the reference "total surface $PM_{2.5}$ concentrations". This method, instead of directly using the $PM_{2.5}$ concentrations from CTL as the reference, removes the slight effect of chemical nonlinearity in source attribution[2,3]. Later, C^{y}_{i} (with y equal to 2014) is compared to satellite-derived surface $PM_{2.5}$, and is employed to establish a conversion map to correct CTM bias (see detailed information in Supplementary Material S3).

$$C^{y}_{i} = C^{y}_{natural,i} + \sum_{g}\sum_{p} C^{y}_{g,p,i} \quad (1)$$

Here, the subscript *g* denotes four country groups, including high-income, upper middle income, lower middle income and low-income group. The subscript *p* denotes $PM_{2.5}$ components, including SIOA (adding up sulfate, nitrate and ammonium), BC, POA, SOA (TSOA + ISOA + ASOA in the model), fine dust (DST1 + 0.38 × DST2 in the model), and fine sea salt particles (SALA in the model), following the model default. The subscript *i* denotes the model grid cell (at a spatial resolution of 2.5° longitude × 2.0° latitude). The superscript *y* denotes the simulation year (1951, 1960, 1970, 1980, 1990, 2000, or 2014).

All simulations are conducted with fixed meteorological conditions in the year of 2014 to better quantify the impacts of anthropogenic emissions. To test the effect of this choice, we conduct sensitivity simulations for 1990 using the meteorology of that year. As shown in Fig. S3, the estimated global premature deaths attributed to each group are comparable (within 8%) by using either the 1990 or 2014 meteorological conditions, so are the estimated nonlocal deaths.

S2. Derivation of consecutive yearly $PM_{2.5}$ concentrations

In this study, the total $PM_{2.5}$ concentrations are contributed by three categories: (1) anthropogenic SIOA, BC and POA, (2) anthropogenic SOA, and (3) natural aerosols. The following describes how each category of $PM_{2.5}$ is derived for each year.

S2.1 Calculation of consecutive yearly anthropogenic SIOA, BC and POA based on chemical efficiencies

For anthropogenic SIOA, BC and POA, we use chemical efficiencies (CEs) and historical anthropogenic emissions to obtain concentrations on a yearly basis, following our previous work[2,3,23]. CEs represent how long each $PM_{2.5}$ components can remain in the atmosphere, after a given amount of its (or its precursors') emissions are released. For BC and POA, their CEs are the same as the residence time in the atmosphere. For SIOA, the CE depends on both the speed of conversion from precursors to SIOA and the residence time of SIOA.

Eq. 2 shows how the CEs of BC, POA and SIOA contributed by the four groups are established based on the model simulations in each simulation year (1951, 1960, 1970, 1980, 1990, 2000 or 2014).

$$CE^{y}_{g,p,i} = C^{y}_{g,p,i} / E^{y}_{g,p'} \qquad (2)$$

Here, the subscript p' denotes the emitted species (NO_x+SO_2+NH_3, BC and POA), and p denotes the respective $PM_{2.5}$ components (SIOA, BC and POA). The subscript *i* denotes the model grid cell and *g* the country group. The superscript *y* denotes the simulation year. $E^{y}_{g,p'}$ represents the total anthropogenic emissions of p' in year *y* in country group *g*, and $C^{y}_{g,p,i}$ represents the concentration of $PM_{2.5}$ component *p* in grid cell *i* caused by $E^{y}_{g,p'}$. Following previous studies[2,3,23], for SIOA, the CE is calculated by dividing the concentration of SIOA (adding up sulfate, nitrate and ammonium) by the sum of emissions of SO_2 (expressed in terms of sulfate), NO_x (expressed in terms of nitrate) and NH_3 (expressed in terms of ammonium), to reduce the nonlinear effect of thermodynamic equilibrium.

Then we employ linear interpolation between two adjacent simulation years to obtain yearly CE of SIOA ($CE^{t}_{g,SIOA,i}$, with *t* ranging from 1950 to 2014), BC ($CE^{t}_{g,BC,i}$) and POA ($CE^{t}_{g,POA,i}$).

For the year of 1950, the CEs in 1951 are directly applied. We subsequently use the interpolated CEs to convert the year- and group-specific anthropogenic emissions to respective gridded concentrations worldwide (Eq. 3).

$$C^{t}_{g,p,i} = CE^{t}_{g,p,i} \times E^{t}_{g,p'} \quad (3)$$

According to our previous studies[2,3], the application of chemical efficiencies introduces slight errors from two aspects. Firstly, the use of CE may lead to a slight error (about 8%) for SIOA due to the thermodynamic interdependence between sulfate, nitrate and ammonium. Secondly, there are multiple regions in each income group, as shown in Fig. S1. It means that the spatial pattern of emissions within each income group may slightly change year to year. However, linear interpolation of CEs between simulation years could reduce this error.

To quantify how the uncertainty in yearly CEs caused by linear interpolation affects the mortality calculation, we further examine three alternative methods to obtain the yearly CEs. Method 1 applies the CEs of a simulation year to all following non-simulation years until the next simulation year. For example, the CEs of 1990 are applied to 1991–1999. Method 2 applies the CEs of a simulation year to all prior non-simulation years until the previous simulation year. For example, the CEs of 2000 are applied to 1991–1999. Method 3 applies the CEs of a simulation year to its closest non-simulation years. For example, the CEs of 1990 are applied to 1991–1994, the CEs of 2000 are applied to 1996–1999, and the average CEs of 1990 and 2000 are applied to 1995. The estimated global population-weighted $PM_{2.5}$ based on these three alternative methods are shown in Fig. S12. On a yearly basis, these alternative methods lead to maximum differences (relative to the above linear interpolation approach) by about 9%, 15%, 5% and 4% for the population-weighted $PM_{2.5}$ attributed to the high-income, upper middle, lower middle and low-income groups, respectively. These errors are embedded in the overall error associated with the use of CEs (σ3, see Supplementary Material S5).

S2.2 Calculation of consecutive yearly anthropogenic SOA

For anthropogenic SOA, we apply linear interpolation to all non-simulation years between two adjacent simulation years to obtain consecutive yearly anthropogenic SOA ($C^{t}_{g,SOA,i}$ in Eq. 4, with *t* ranging from 1950 to 2014). For 1950, we use the SOA in 1951 directly. Then, the

anthropogenic $PM_{2.5}$ at the model grid cell *i* contributed by country group *g* in year *t* can be obtained (Eq. 4). The subscript *p* denotes SIOA, BC and POA.

$$C_{g,i}^{t} = C_{g,SOA,i}^{t} + \sum_{p} C_{g,p,i}^{t} \qquad (4)$$

For a sensitivity test, we adopt the CE based approach (same as that for SIOA, BC and POA) to calculate yearly SOA, with the CE calculated as anthropogenic SOA (TSOA+ISOA+ASOA in the model) concentrations divided by anthropogenic NMVOC emissions. Figure S4 shows that the annual mean global population-weighted SOA concentrations caused by any income group are similar (with NRMSD within 2–7%) between the direct interpolation and the CE based method.

GEOS-Chem and most other CTMs tend to underestimate SOA concentrations[24]. Over anthropogenic emission-heavy regions like eastern China, total (anthropogenic + natural) SOA contribute about 15-30% of the total annual surface $PM_{2.5}$[24-26]; and anthropogenic emissions are more important than biogenic sources. In other regions like the US, SOA is mainly contributed by biogenic sources; and the contributions of anthropogenic SOA to total $PM_{2.5}$ are on the order of 10%[27-29]. Our present study focuses on anthropogenic impacts, thus using either the interpolation- or CE-based method to calculate SOA has a minor effect on our analysis of anthropogenic premature mortality.

S2.3 Natural and total $PM_{2.5}$

Natural emissions of $PM_{2.5}$ and precursors are shown in Table S1. Natural emissions are determined by meteorological conditions, leaf area index (LAI, affecting biogenic NMVOC and soil NOx emissions), and biomass burning. We fix the meteorological conditions at the 2014 level, but allow LAI and biomass burning to change slightly (see the footnote of Table S1). The changes in LAI and biomass burning have insignificant effects (within 2%) on the simulated natural $PM_{2.5}$ concentrations. Thus, in effect, the simulated natural $PM_{2.5}$ represents the situation in 2014. Nevertheless, we employ linear interpolation to derive natural $PM_{2.5}$ for non-simulation years and thus obtain consecutive yearly natural $PM_{2.5}$ data ($C_{natural,i}^{t}$, with t ranging from 1950 to 2014), as done for SOA. Therefore, the total $PM_{2.5}$ concentration in year *t* at model grid cell *i* (C_i^t) can be obtained by Eq. 5. Here the subscript *g* denotes the income group. Later, C_i^t is corrected and validated based on satellite-derived surface $PM_{2.5}$ data (see Supplementary

Material S3), with corrected $PM_{2.5}$ used to estimate premature deaths (see Supplementary Material S4).

$$C_i^t = C_{natural,i}^t + \sum_g C_{g,i}^t \qquad (5)$$

S3. GEOS-Chem evaluation and adjustment

The $PM_{2.5}$ simulation by GEOS-Chem has been evaluated extensively by previous studies[2,12,14,30], including comparisons with ground, satellite and airborne measurements. Here, we briefly compare the simulated surface $PM_{2.5}$ with satellite-derived $PM_{2.5}$ data worldwide and derive scaling factors to correct systematic model biases on a grid cell basis. The satellite-derived $PM_{2.5}$ data are estimated by combining satellite retrieved aerosol optical depth and GEOS-Chem model, with further calibration based on massive global ground-based $PM_{2.5}$ observations and geographically weighted regression.

We compare the explicitly simulated (i.e., without application of CEs) annual mean population-weighted $PM_{2.5}$ with the satellite-derived $PM_{2.5}$ concentrations (V4.GL.02)[31] over 12 main regions and the globe for 2014 (Fig. S13) and 2000 (Fig. S14). We re-grid the satellite-derived $PM_{2.5}$ concentrations from its original horizontal resolution (0.1° longitude x 0.1° latitude) to model resolution (2.5° longitude × 2.0° latitude) to facilitate the comparison. Examination of population-weighted $PM_{2.5}$ allows focused model evaluation over densely populated areas. In 2014 (Fig. S13), the simulated $PM_{2.5}$ concentrations are consistent with satellite-derived data, with R^2 of 0.83–0.98 and NRMSD of 1.6%–7.8% across the regions. In 2000 (Fig. S14), R^2 ranges from 0.79 to 0.99 and NRMSD from 1.7% to 8.0%. The NRMSD in China in 2000 (8.0%) is the largest among the regions in the two years; and this value is used to present the random part of CTM errors (σ2, see Supplementary Material S5) not captured by the following satellite-based correction.

We correct the systematic CTM bias using the satellite-derived $PM_{2.5}$ data. We calculate the ratio of satellite-derived to simulated $PM_{2.5}$ concentrations for each grid cell in 2014 (Eq. 6), and subsequently apply the gridded ratios to all years over 1950–2014 (Eq. 7).

$$R_j^b = C_j^{s,b} / C_i^b \qquad (6)$$

$$C_j^t = R_j^b \times C_i^t \qquad (7)$$

Here the superscript *b* denotes the year of 2014, *t* the year between 1950 and 2014, and *s* the satellite-based data. $C_j^{s,b}$ denotes the satellite-derived $PM_{2.5}$ at grid cell *j* on the 0.1° longitude × 0.1° latitude grid; and C_i^t denotes the pre-adjusted $PM_{2.5}$ on the 2.5° longitude × 2.0° latitude grid. The center of the finer grid cell *j* is located in the coarser grid cell *i*.

Comparison of the resulting yearly $PM_{2.5}$ concentrations (C_j^t in Eq. 7) with the satellite-derived data over 2000–2013 on the 0.1° longitude × 0.1° latitude grid shows R^2 of 0.91–0.99 and NRMSD within 1% (see details in Table S2). This supports the robustness of our correction method.

It is worthy to note that the simulated $PM_{2.5}$ concentrations are obtained using GEOS-Chem with fixed meteorological conditions, and the satellite-derived $PM_{2.5}$ data represent real-world concentrations with meteorological effects. Despite all this, the comparison in this study is still valid because the meteorological effects are small when focusing on annual mean $PM_{2.5}$ concentrations and the related health impacts, which could be supported by Fig. S3, Fig. S14 and Table S2.

S4. Premature deaths caused by ambient $PM_{2.5}$ exposure

We use the GEMM model[32] to estimate the $PM_{2.5}$-related premature deaths. All mortality results presented in the main text are based on the GEMM NCD+LRI method[32], which link the deaths due to non-communicable diseases (NCDs) and lower respiratory infections (LRIs) associated with ambient $PM_{2.5}$ exposure.

To derive the mortality, we use the country-, year-, age- and disease-specific baseline mortality data from the GBD2017 database[33], which are available since 1990. We take the country-, year-, and age-specific population data from the World Population Prospects 2019 (WWP)[34], which are available since 1950. We calculate the baseline mortality rates since 1990 from the above population data and baseline mortality data. The baseline mortality rates in 1990 are applied to all prior years due to data limitation. Following previous studies[2,3], we assume the age-, year-, disease- and country-specific baseline mortality rate remains unchanged within each country, and assume the age-, year- and country-specific age-structure remains unchanged within each country.

To calculate the mortality for each grid cell, we further adopt the gridded population distribution on a 0.1° x 0.1° grid from the GBD2016 health database for the years of 1990, 1995, 2000, 2005, 2010, 2011, 2012, 2013 and 2014. For the years with available gridded GBD population databases, we use the country-based WPP data to adjust the GBD data within each country. For the years without gridded GBD population databases (e.g., 2001), we apply linear interpolation to obtain the horizontal distributions. The horizontal shape of population in 1990 is applied to prior years.

Following previous studies[2,14,35], we attribute the total $PM_{2.5}$-related premature deaths to each source by a direct proportion approach, which assumes that the contribution of each pollution source to the health burden of that pollution is the same as the contribution of that source to the pollution concentration.

We test the effect of using fixed baseline mortality rates for the years prior to 1990, by applying the trends of the rates either over 1990–2000 or over 1990–2014 to prior years following a previous study[36]. These alternative methods lead to slight differences in the calculated mortality numbers (within 10% for global annual total, Fig. S5).

We compare our GEMM NCD+LRI based results with previous studies using the same exposure-response model[2,3,32,37] (Fig. S8b). The results in this study are consistent with our two previous studies[2,3]. The differences (within 20%) in global mortality between our results and those from Burnett et al.[32] (for 2015) and Chowdhury et al.[37] (for 2000 and 2015) mainly reflect the updated baseline mortality data used here, as detailed in Supplementary Data 2 of Lin et al.[2]. In addition, we estimate the premature mortality on a grid cell basis using location-specific $PM_{2.5}$ concentrations, instead of using the national average $PM_{2.5}$ concentrations, as done in Burnett et al.[32] and Chowdhury et al.[37].

To further examine the effects of exposure-response model used, we employ the Integrated Exposure-Response model (IER)[38] as a sensitivity test to re-estimate the $PM_{2.5}$-related mortality. We then compare the resulting mortality numbers to previous IER-based studies (Fig. S8a). Our results here are consistent with our two previous studies for 2014[2,3] and Lelieveld et al. for 2010[39]. The mortality estimate by Butt et al.[36] for 1960–2009 based on un-corrected UKCA climate model simulations of $PM_{2.5}$ (the pink line in Fig. S8a) is systematically lower than ours (the black line), although with similar trends, mainly because of their underestimate of

$PM_{2.5}$ concentrations. Their test using the GBD PM data (the green line in Fig. S8a) shows global mortality close to ours for 1990–2010. In addition, the mortality calculation is subject to continuously updates of IER parameters and baseline mortality data. As evident from Fig. S8a, the multiple GBD studies themselves show notable differences in the estimated mortality[40-44]. Our mortality estimate differs from Zhang et al.[14] for 2007 and Shindell et al.[45] for 2010 because these two studies employ older versions of IER parameters and baseline mortality data from GBD2010[38,43] whereas we employ the parameters from GBD2016[42] and the baseline mortality data from GBD2017[44]. Our calculated mortality trend is consistent with GBD2017[44] and GBD2016[42]. Overall, all the differences discussed above are within the uncertainty range of our study.

Note that compared to IER, GEMM NCD+LRI is built purely based on cohort studies of outdoor air pollution that covers much of the range of ambient $PM_{2.5}$ concentrations worldwide[32]. Different from five specific diseases included in IER, GEMM NCD+LRI considers all non-communicable diseases and LRIs[32]. Thus GEMM NCD+LRI results in a systematically higher estimate of mortality than IER[32]. Our previous test shows that using the GEMM model but including the five diseases only would lead to global mortality lower than that based on GEMM NCD+LRI by 32% but higher than the IER-based result by 43% (Supplementary Data 2 of Lin et al.[2]). However, for the analysis of transboundary mortality and embedded inequality, the choice of exposure-response model (IER or GEMM) has little effect on the conclusion.

We further compare the transboundary health impacts calculated in this study with previous studies. The annual contribution of transboundary deaths to $PM_{2.5}$-associated global total deaths ranges from 12% to 15% over 1950–2014, with an average value at 14%. These values are comparable to Zhang et al.[14] focusing on the year of 2007 (12%). We also compare our results with the transboundary studies in HTAP which focused on the years of 2001[46] and 2010[47]. The HTAP studies modeled the response of worldwide $PM_{2.5}$ pollution and mortality to a 20% emission reduction in each source region, a source-receptor analysis approach which is different from our source attribution approach based on “zero-out” simulations. Zhang et al.[14] showed that the transboundary impact fraction based on the “zero-out” method is about 2.4 times of that based on “20% emission reduction” (i.e., 12% versus 5%). This difference can be explained by the nonlinearity in model chemistry (i.e., conversion from emissions to concentrations) and

pollution exposure-response functions. Scaling the transboundary impact fractions derived in the two HTAP studies by a factor of 2.4 (to approximate the fractions based on "zero-out" simulations) would lead to a transboundary impact fraction in 2001 at 15.9% (scaled from 6.6% in Anenberg et al.[46]), and at 10.2% in 2010 (scaled from 4.3% in Liang et al.[47]). These scaled fractions are comparable to the results in this study.

S5. Uncertainty

Our calculated mortality results are affected by errors in anthropogenic emissions (σ1, as one standard deviation), GEOS-Chem simulations (σ2), application of chemical efficiencies and linear interpolation (σ3), and GEMM NCD+LRI pollution exposure-response modeling (σ4). See detailed discussion about these uncertainty sources in our previous study[2]. Briefly, the emission errors (σ1) are embedded in GEOS-Chem simulations (σ2). Based on the comparison of GEOS-Chem simulated $PM_{2.5}$ concentrations against satellite-based data for 12 individual regions in 2014 (Fig. S13) and 2000 (Fig. S14), we use the NRMSD in China in 2000 (8%, the largest value among the 12 regions in the two years) to represent the random part of CTM errors not captured by the satellite-based correction. Following our previous study[2,3,23], we assign a 15% error to σ3. We apply the uncertainty ranges of individual parameters in GEMM[32] to quantify σ4. The overall uncertainty in $PM_{2.5}$-related annual premature deaths is calculated as the sum in quadrature of σ2 (the random part), σ3 and σ4. All the factors overall introduce a 38% error (two standard deviations) to our best estimates of premature deaths presented in the main text.

S6. Decomposition of anthropogenic $PM_{2.5}$-related premature deaths

We employ a decomposition method to decompose the anthropogenic $PM_{2.5}$-related premature deaths into the individual effects of three factors, including baseline mortality rate (B), exposed population (POP, including size and age structure) and $PM_{2.5}$ pollution (PM). According to the function of GEMM NCD+LRI, the change in anthropogenic $PM_{2.5}$-related premature mortality (M) from one year to another can be decomposed as:

$$\Delta M = \Delta B \times POP \times PM + B \times \Delta POP \times PM + B \times POP \times \Delta PM \quad (8)$$

Here, ΔM denotes the change in anthropogenic premature deaths. Each of the three terms on the right-hand side of the Eq. 8 denotes the contribution of baseline mortality rate, population, and $PM_{2.5}$ pollution, respectively.

Our decomposition method is similar to Structural Decomposition Analysis (SDA) which is a widely used approach to break down the observed changes in physical variables like energy consumption or CO_2-emissions into the changes in its determinants[48-52]. Similar to conducting an SDA, evaluating different terms for the start or end point of the investigated time period is possible. Considering that there are three factors in Eq. 8, there are 3! = 6 possible first-order decompositions, which are all used in this study to derive the averaged decomposition results.

Supplementary Tables

Table S1: Emissions used in this study.

Region	Inventory	Resolution[a]	Year	Species[b]	References and notes
Anthropogenic emissions					
Global	CEDS	0.5°×0.5°, monthly	1950-2014	BC, CO, NH_3, NO_X, SO_2, OC, NMVOC	Hoesly et al.[18]
Global	AEIC, aircraft	1°x 1°, annual	2005	NO, SO_2, CO, BC, OC, NMVOC	Simone et al.[53]
Global	ARCTAS, shipping	1°x 1°, annual	2008	SO_2	Eyring et al.[54,55]
Global	ICOADS, shipping	1°x 1°, monthly	2002	CO, NO	Wang et al.[56]
Europe	EMEP_shipping	1°x 1°, annual	2012	CO, SO_2, NO	https://www.ceip.at[57]
China[d]	MEIC	0.25°x0.25°, monthly	2000-2014	NOx, CO, SO_2, BC, OC, NH_3, NMVOC[c]	MEIC web[20]; Geng et al.[19]; Li et al.[21]; Zheng et al.[22]
Other emissions					
Global	GFED4 biomass burning	0.25°x0.25°, monthly	Year-specific[e]	NO, CO, NMVOC, SO_2, NH_3, BC, OC, POG1, POG2, NAP	Giglio et al.[58]
Global	MEGAN biogenic NMVOC	Model resolution	Year-specific[f]	ISOP, ACET, PRPE, C_2H_4, ALD2	Guenther et al.[59]
Global	Soil NOx	Model resolution	2014	NO	Hudman et al.[60]
Global	Lightning NOx	Model resolution	2014	NO	Murray et al.[61]
Global	DEAD	Model resolution	2014	Mineral dust	Fairlie et al.[62,63], Zhang et al.[64]
Global	Jaeglé et al.	Model resolution	2014	Sea salt	Jaeglé et al.[65]

[a] Before re-gridded to model horizontal resolutions. For more information, see http://wiki.seas.harvard.edu/geos-chem/index.php/Anthropogenic_emissions.
[b] Notes for NMVOC: CEDS includes C_2H_6, C_3H_8, ALK4, C_2H_4, PRPE, C_2H_2, BENE, TOLU, XYLE, CH_2O, ALD2 and MEK. In GEOS-Chem, MEK emissions are further allocated to MEK (25%) and ACET (75%). MEIC includes PRPE, MEK, CH_2O, C_3H_8, C_2H_6, ALK4, ALD2, ACET.
[c] We apply a scale factor (i.e., the ratio between the total NMOVC emission in 2014 and that in 2012) to each gridded NMVOC species in 2012 to obtain the respective gridded emission in 2014.
[d] The CEDS emission data are replaced by MEIC over China area from 2000 to 2014.
[e] The simulations prior to 2000 employ the GFED4 data in 1997, and the simulations in 2000 and 2014 use the year-specific GFED4 data.
[f] MEGAN uses the MODIS LAI data. The LAI data for 2005 are used for simulations in 2000 and prior years, and the LAI data for 2008 are employed for simulations in 2014.

Table S2: Comparison between simulated and satellite-derived population-weighted surface $PM_{2.5}$ concentrations (μg/m³) from 2000 to 2014. The comparisons conducted at a 2.5°x 2.0° resolution employ the reference $PM_{2.5}$ (as shown in Eq. 1) simulated by GEOS-Chem . The comparisons conducted at a 0.1°x 0.1° resolution employ the corrected and CEs-based $PM_{2.5}$ concentrations. The comparison method is the same with Fig. S13 and Fig. S14. Regions include China (CH), rest of East Asia (EA), South Asia (SA), South-East Asia and Pacific (SE), Economics in Transition (ET), Western Europe (WE), the United States (US), rest of North America (NA), Middle East and North Africa (MN), Latin America and Caribbean (LA), Sub-Saharan Africa (SS), Japan and Korea + Oceania (JO) and the whole world. The NRMSD is expressed as percentage.

		CH	EA	SA	SE	ET	WE	US	NA	MN	LA	SS	JO	World
2000 (at 2.5°x 2.0°)	R^2	0.96	0.99	0.93	0.79	0.91	0.94	0.96	0.97	0.93	0.96	0.97	0.97	0.90
	NRMSD	8.0	2.2	7.4	7.7	3.3	7.9	3.4	1.7	4.7	1.9	2.2	2.5	1.8
2000 (at 0.1°x 0.1°)	R^2	0.98	1.00	0.98	0.96	0.99	0.91	0.99	0.99	0.99	0.99	0.96	1.00	0.97
	NRMSD	0.4	0.2	0.3	0.7	0.1	1.1	0.2	0.2	0.1	0.2	0.2	0.1	0.1
2001 (at 0.1°x 0.1°)	R^2	0.98	1.00	0.98	0.98	0.99	0.91	0.99	1.00	0.99	0.99	0.98	1.00	0.98
	NRMSD	0.3	0.2	0.3	0.4	0.1	1.0	0.1	0.1	0.1	0.1	0.2	0.1	0.1
2002 (at 0.1°x 0.1°)	R^2	0.99	1.00	0.98	0.98	0.99	0.93	0.99	1.00	0.99	0.99	0.98	1.00	0.98
	NRMSD	0.3	0.1	0.3	0.4	0.1	0.8	0.1	0.3	0.1	0.1	0.2	0.1	0.1
2003 (at 0.1°x 0.1°)	R^2	0.99	1.00	0.98	0.98	0.99	0.91	0.99	0.98	0.99	0.99	0.99	1.00	0.98
	NRMSD	0.3	0.2	0.3	0.4	0.1	0.9	0.1	0.3	0.1	0.1	0.1	0.1	0.1
2004 (at 0.1°x 0.1°)	R^2	0.99	1.00	0.99	0.98	0.99	0.93	0.99	0.99	0.99	0.99	0.98	1.00	0.98
	NRMSD	0.3	0.2	0.3	0.4	0.1	1.0	0.1	0.3	0.1	0.1	0.2	0.2	0.1
2005 (at 0.1°x 0.1°)	R^2	0.99	1.00	0.99	0.99	0.98	0.93	0.99	0.99	0.99	0.99	0.97	1.00	0.99
	NRMSD	0.2	0.3	0.2	0.3	0.1	1.0	0.1	0.2	0.1	0.1	0.2	0.2	0.1
2006 (at 0.1°x 0.1°)	R^2	0.99	1.00	0.99	0.98	0.97	0.91	1.00	0.99	0.99	1.00	0.98	1.00	0.99
	NRMSD	0.3	0.2	0.2	0.4	0.2	0.8	0.1	0.2	0.1	0.1	0.2	0.2	0.1
2007 (at 0.1°x 0.1°)	R^2	0.99	1.00	0.99	1.00	0.99	0.91	0.99	1.00	0.99	1.00	0.98	1.00	0.99
	NRMSD	0.2	0.3	0.2	0.3	0.1	1.0	0.1	0.1	0.1	0.1	0.2	0.1	0.1
2008 (at 0.1°x 0.1°)	R^2	1.00	1.00	0.98	1.00	0.98	0.93	0.99	1.00	0.97	1.00	0.96	1.00	0.98
	NRMSD	0.2	0.2	0.3	0.3	0.1	1.0	0.2	0.2	0.2	0.1	0.2	0.1	0.1
2009 (at 0.1°x 0.1°)	R^2	1.00	1.00	0.99	0.99	0.99	0.93	1.00	0.99	0.98	1.00	0.99	1.00	0.99
	NRMSD	0.2	0.1	0.2	0.4	0.1	0.8	0.2	0.2	0.2	0.1	0.1	0.1	0.1
2010 (at 0.1°x 0.1°)	R^2	1.00	1.00	0.99	0.99	0.99	0.91	1.00	0.99	0.99	0.99	0.98	1.00	0.99
	NRMSD	0.2	0.5	0.2	0.3	0.1	0.9	0.2	0.2	0.1	0.1	0.2	0.2	0.1
2011 (at 0.1°x 0.1°)	R^2	1.00	1.00	0.99	0.99	0.99	0.92	0.99	1.00	0.98	0.99	0.99	1.00	0.99
	NRMSD	0.3	0.6	0.2	0.6	0.1	0.8	0.1	0.1	0.2	0.1	0.1	0.4	0.1
2012 (at 0.1°x 0.1°)	R^2	1.00	1.00	1.00	1.00	0.99	0.93	1.00	1.00	0.98	0.99	0.98	1.00	0.99
	NRMSD	0.4	0.9	0.2	0.2	0.1	0.8	0.1	0.1	0.2	0.1	0.2	0.4	0.1
2013 (at 0.1°x 0.1°)	R^2	0.99	1.00	0.99	1.00	0.99	0.94	1.00	1.00	0.99	0.99	0.99	1.00	0.99
	NRMSD	0.2	0.1	0.2	0.2	0.1	0.6	0.1	0.1	0.1	0.1	0.1	0.1	0.1
2014 (at 0.1°x 0.1°)	R^2	1.0	1.0	1.0	1.0	1.0	1.0	1.0	1.0	1.0	1.0	1.0	1.0	1.0
	NRMSD	0	0	0	0	0	0	0	0	0	0	0	0	0
2014 (at 2.5°x 2.0°)	R^2	0.94	0.99	0.96	0.83	0.90	0.89	0.98	0.95	0.95	0.95	0.94	0.98	0.94
	NRMSD	6.4	3.7	7.0	7.8	3.5	6.1	3.6	2.5	4.1	2.0	3.9	2.2	1.6

Supplementary Figures

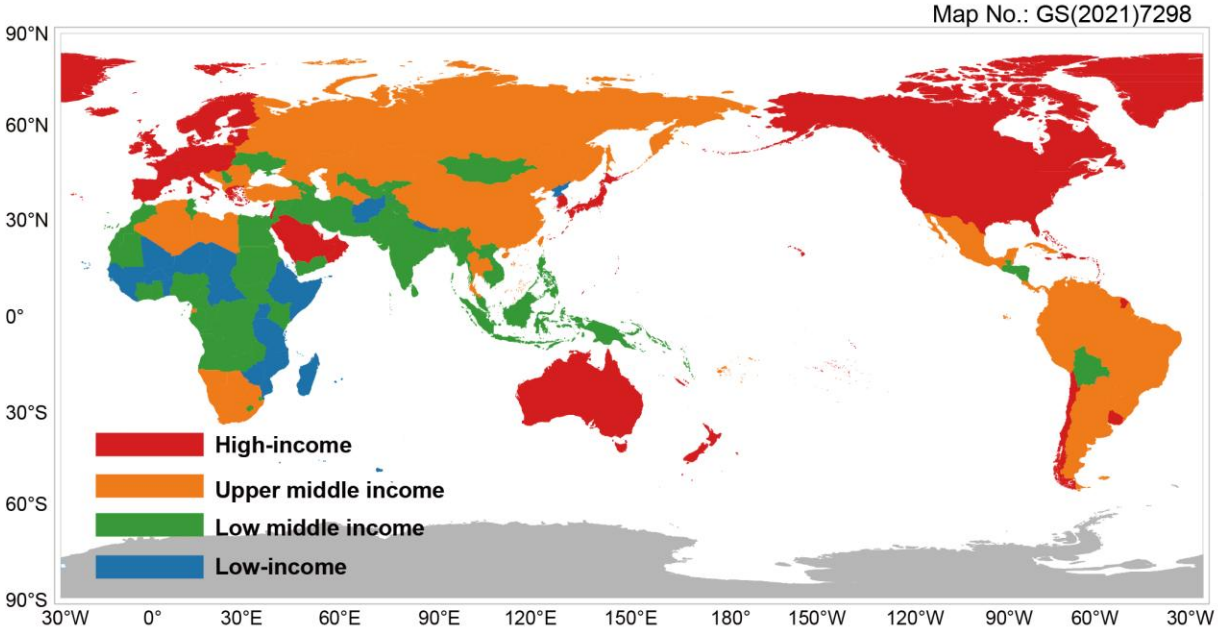


Fig. S1. Income group classification. The classification of country groups follows the World Economic Situation Prospects 2018[66], including high-income, upper middle income, lower middle income and low-income.

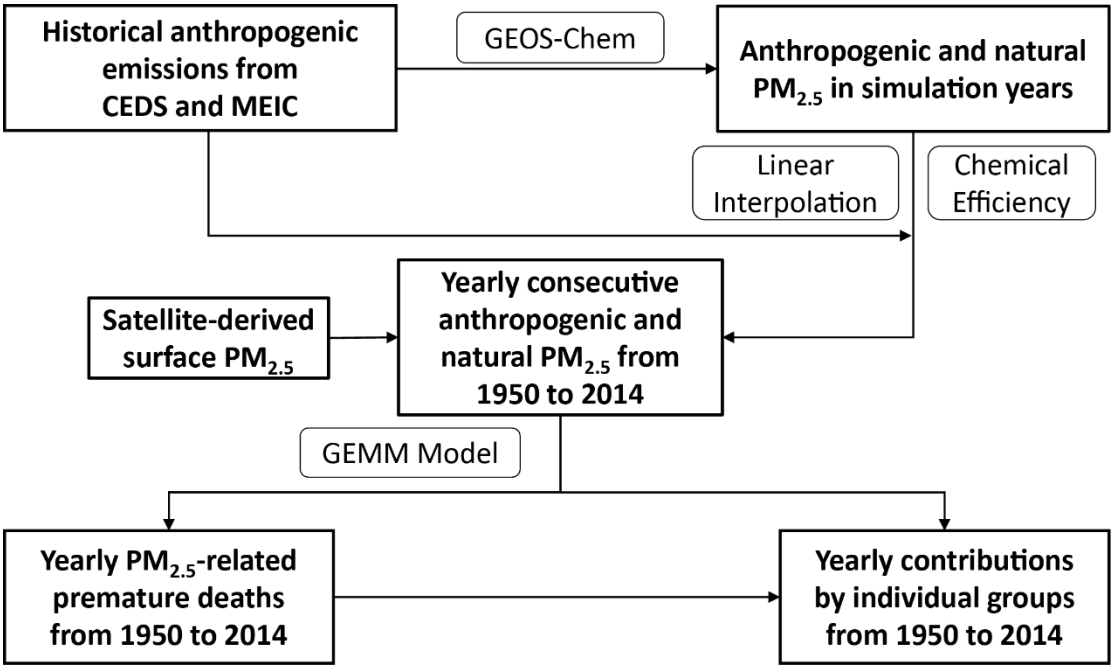


Fig. S2. Methodological flowchart to calculate yearly mortality.

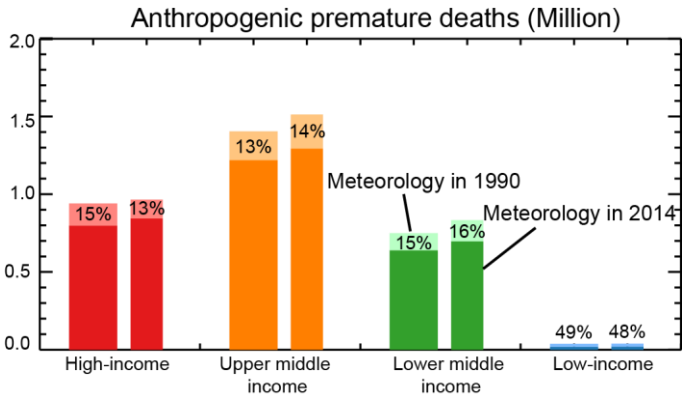


Fig. S3. Annual anthropogenic $PM_{2.5}$-related premature deaths caused by four income groups in 1990. The wider bars are obtained based on GEOS-Chem simulations driven by meteorological conditions in 1990. The narrower bars are based on simulations driven by meteorological conditions in 2014. The numbers represent the percentage contributions of nonlocal premature deaths (denoted by light colors) to total global premature deaths caused by anthropogenic emissions in the individual groups.

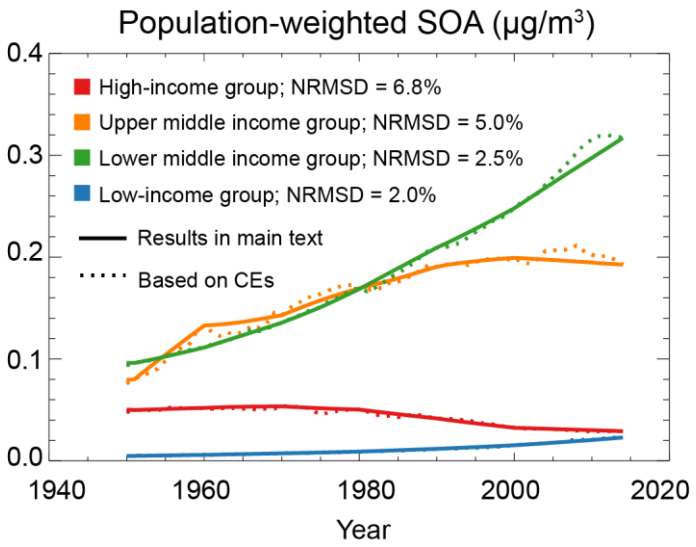


Fig. S4. Historical changes in annual mean global population-weighted SOA concentrations caused by four groups. The solid lines represent the estimation in the main text (i.e., directly applying linear interpolation between two adjacent simulation years). The dot lines indicate the estimation based on chemical efficiencies (see Supplementary Material S2.2).

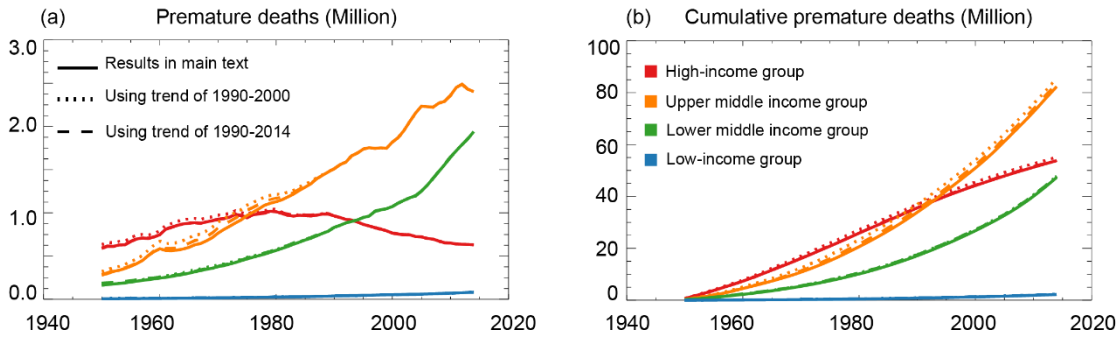


Fig. S5. Historical changes in annual anthropogenic $PM_{2.5}$-related premature deaths. The y-axis shows the historical yearly anthropogenic premature deaths (a) and cumulative premature deaths (b) caused by the four groups. The solid lines represent the estimation in the main text (i.e., applying the baseline mortality rates at 1990 to all prior years). The dot lines and dash lines are calculated with the baseline mortality rates before 1990 extrapolated based on the country-specific trends over 1990–2000 and over 1990–2014, respectively.

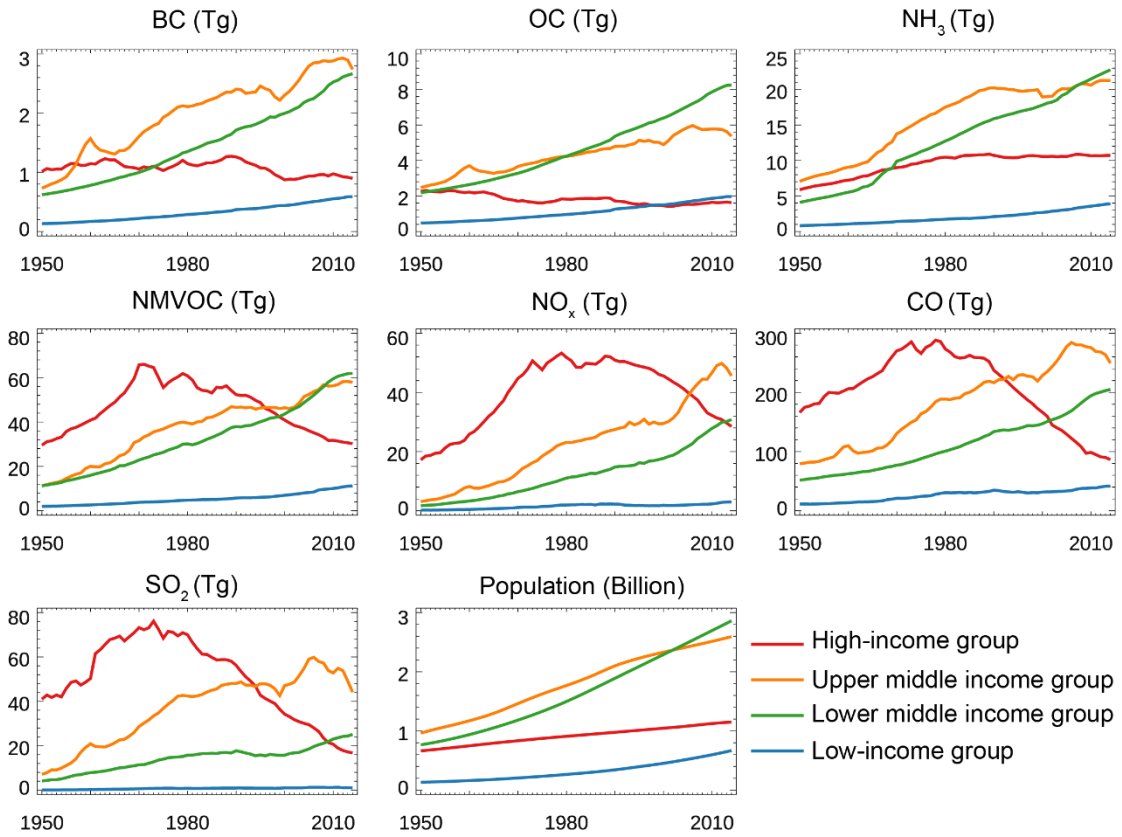


Fig. S6. Historical annual anthropogenic emissions and population of four groups. The anthropogenic emissions are taken from CEDS[18], with emissions of China from 2000 to 2014 replaced by MEIC[19-22]. Population data are taken from the WPP[34].

400

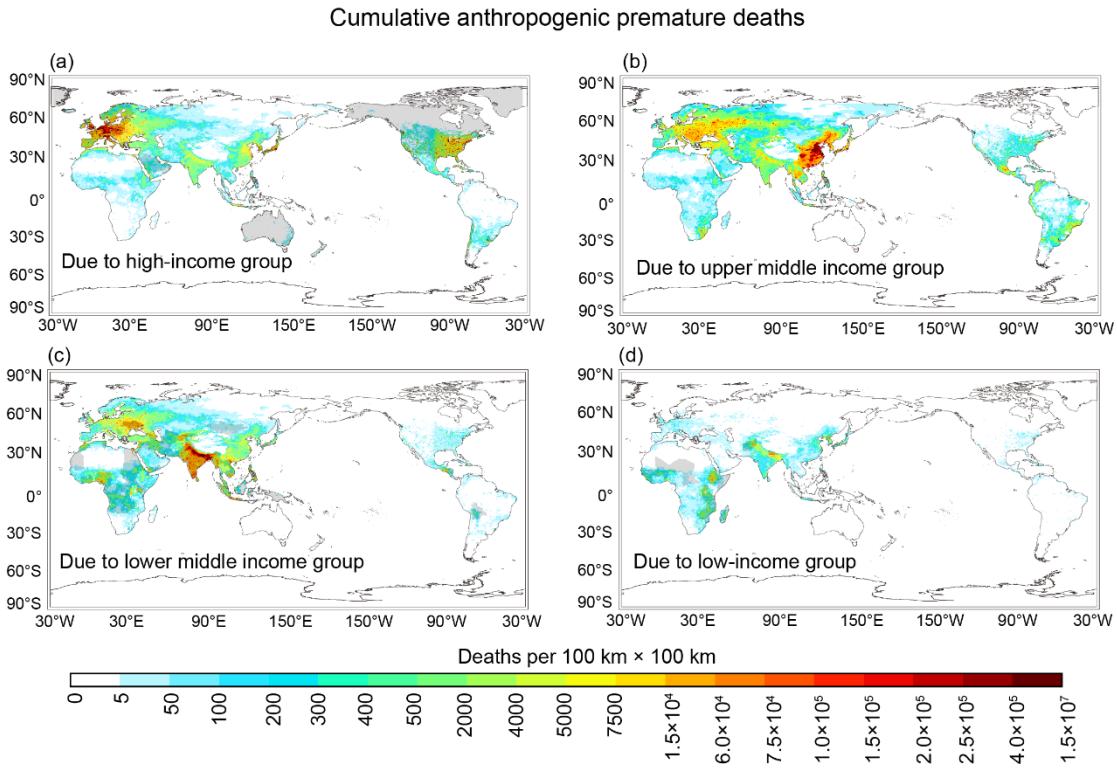


Fig. S7. Spatial distributions of cumulative premature deaths from 1950 to 2014. The cumulative premature deaths caused by anthropogenic emissions in the high-income (a), upper middle (b), lower middle (c) and low-income (d) groups. The source region in each panel is indicated by grey area.

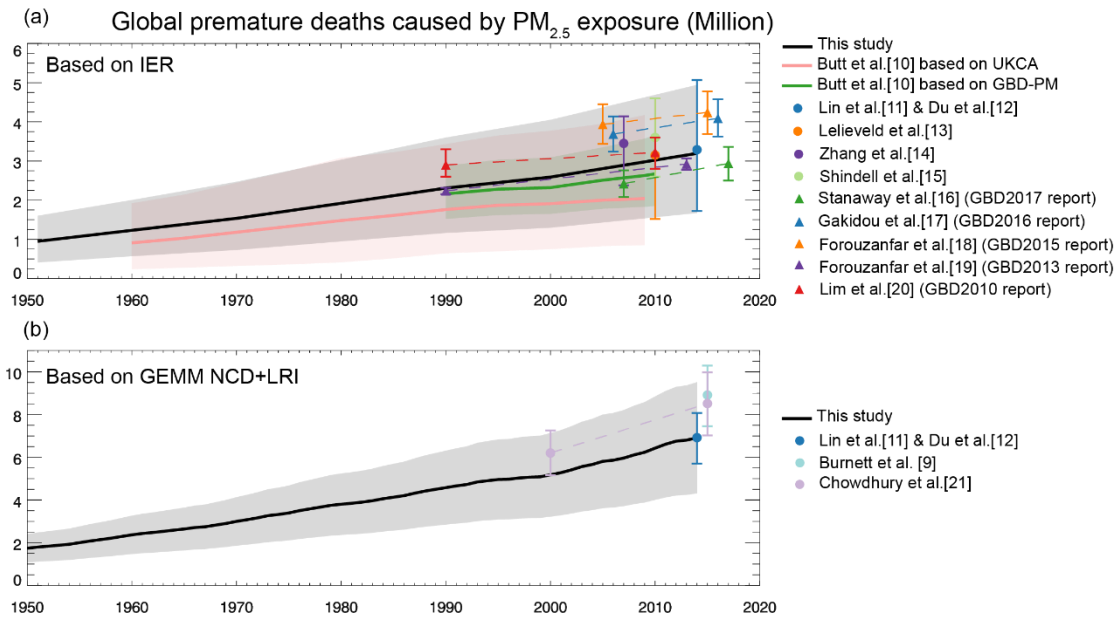


Fig. S8. Comparison between our annual mortality results and previous findings. The $PM_{2.5}$-related premature deaths estimated based on the exposure-response models of IER[38] (a) and GEMM NCD+LRI[32] (b). The black shadow denotes 95% CI of this study. The pink and green lines represent the median estimates based on UKCA and GBD-PM in Butt et al.[36], and pink and green shadows denote the corresponding uncertainty ranges. Previous studies include Lin et al.[2], Du et al.[3], Lelieveld et al.[39], Zhang et al.[14], Shindell et al.[45], Stanaway et al.[44], Gakidou et al.[42], Forouzanfar et al[40]., Forouzanfar et al.[41], Lim et al.[43], Burnett et al.[32], and Chowdhury et al.[37].

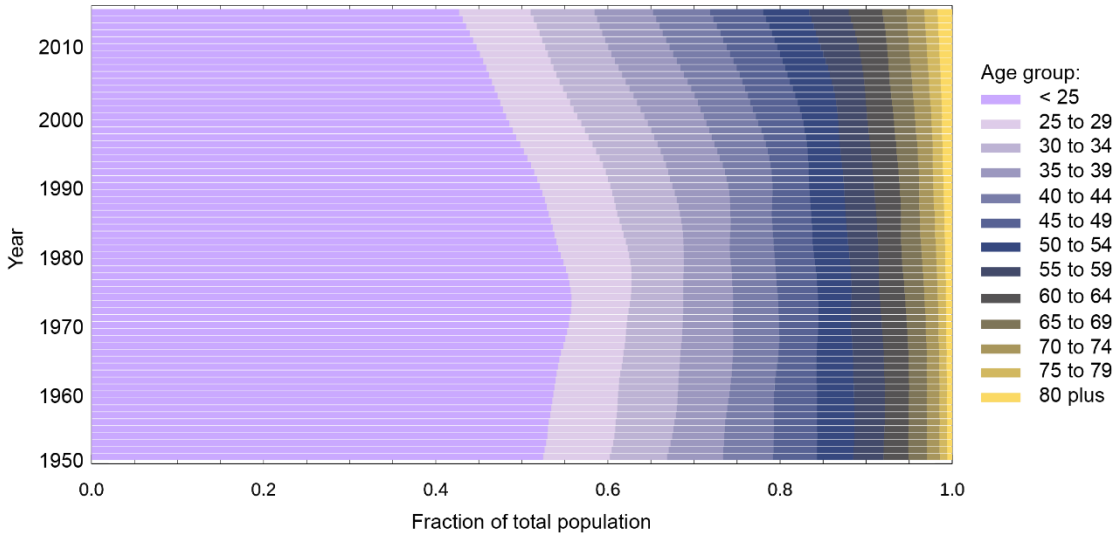


Fig. S9. Historical changes in global age structure. Population data are taken from the WPP[34].

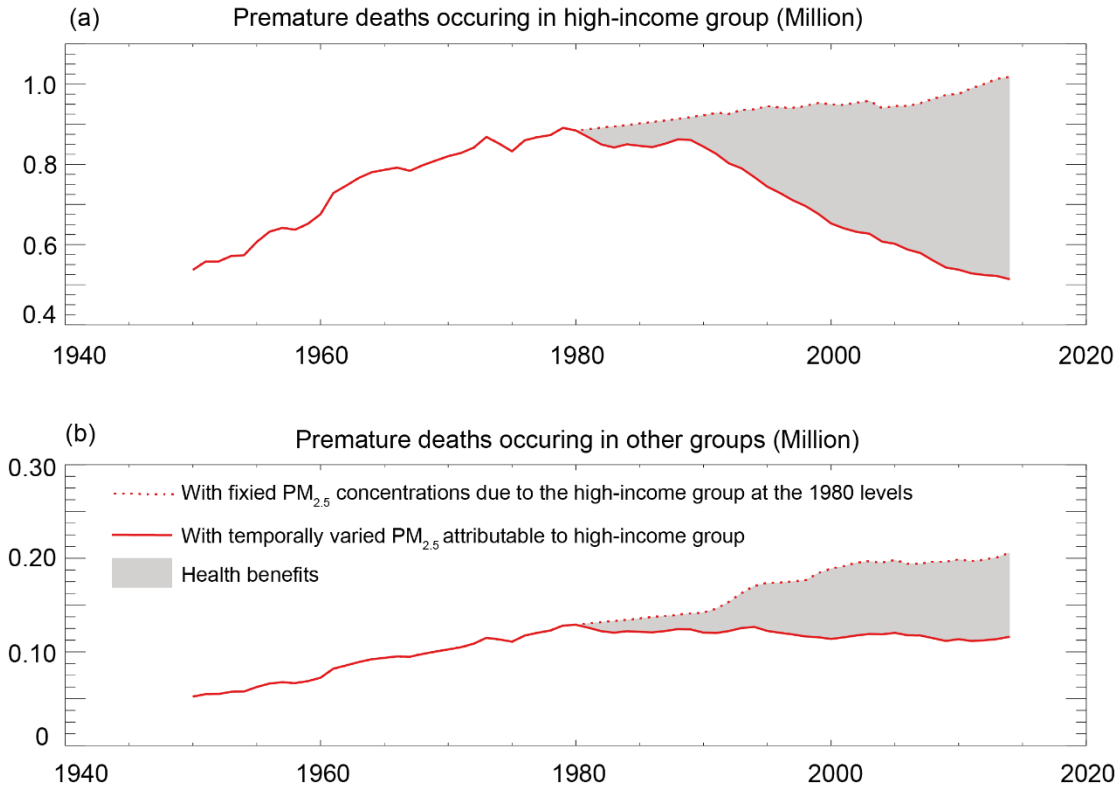


Fig. S10. Annual premature deaths attributable to anthropogenic emissions in high-income group. The premature deaths occurring in the high-income group (a) and in the other three groups (b). The solid line represents the premature deaths caused by the high-income group driven by their emission changes. The dotted line shows results of a sensitivity study for 1980–2014, by fixing $PM_{2.5}$ concentrations contributed by the high-income group at the 1980 levels. The shaded area represents the avoided deaths because of emission control in the high-income group.

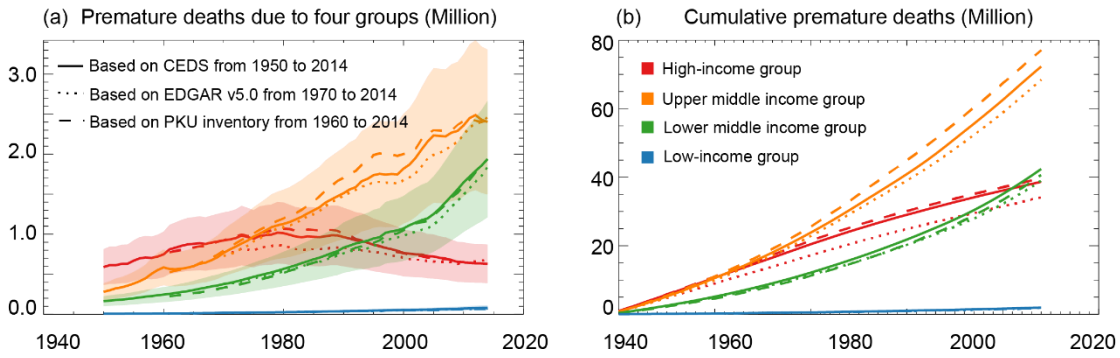


Fig. S11. Historical changes in anthropogenic $PM_{2.5}$-related premature mortality. The yearly (a) and cumulative (b) premature deaths caused by anthropogenic emissions in the four groups. The solid lines represent the results based on CEDS[18]+MEIC[19-22]. The dot and dash lines indicate the results based on EDGAR v5.0[67] and the PKU inventory[68-72], respectively. The shadow areas in (a) indicate the 95% CI of the CEDS+MEIC based estimate. The EDGAR and PKU based estimates adopt the natural $PM_{2.5}$ from the CEDS+MEIC based estimate, followed by scaling of anthropogenic $PM_{2.5}$ so that the total $PM_{2.5}$ matches the satellite-based data in 2014. In (b), the cumulative premature deaths are calculated with 1970 as the start year, different from Fig. 1a in the main text, because the EDGAR data are available since 1970. In (b), the cumulative mortality results based on the three emission inventories undergo similar patterns.

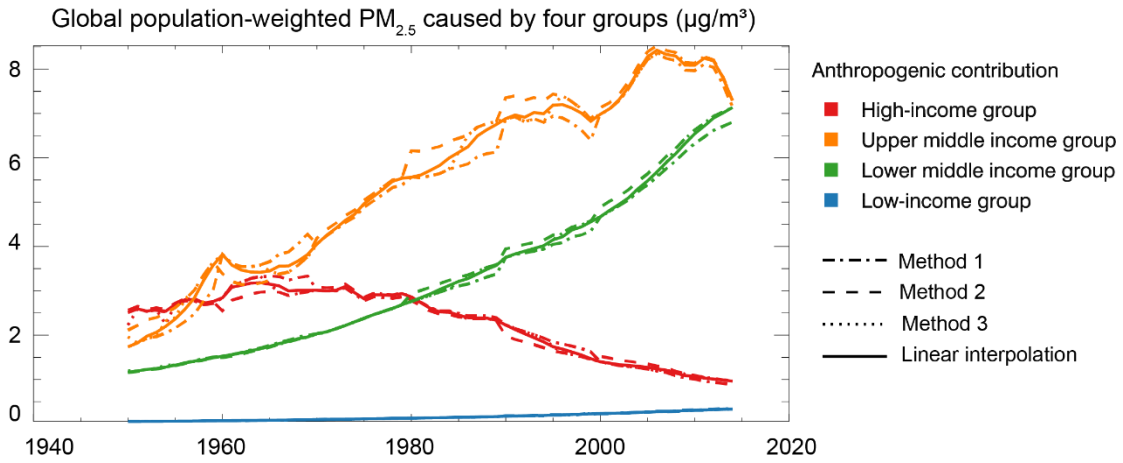


Fig. S12. Historical changes in annual mean global population-weighted $PM_{2.5}$ concentrations caused by anthropogenic emissions in four groups. Population-weighted $PM_{2.5}$ concentrations in different lines are based on CEs obtained by different methods. Method 1 applies the CEs of a simulation year to all following non-simulation years until the next simulation year. Method 2 applies the CEs of a simulation year to all prior non-simulation years until the previous simulation year. Method 3 applies the CEs of a simulation year to its closest non-simulation years. Linear interpolation, as used in the main text, linearly interpolates the CEs of two adjacent simulation years to all non-simulation years in between.

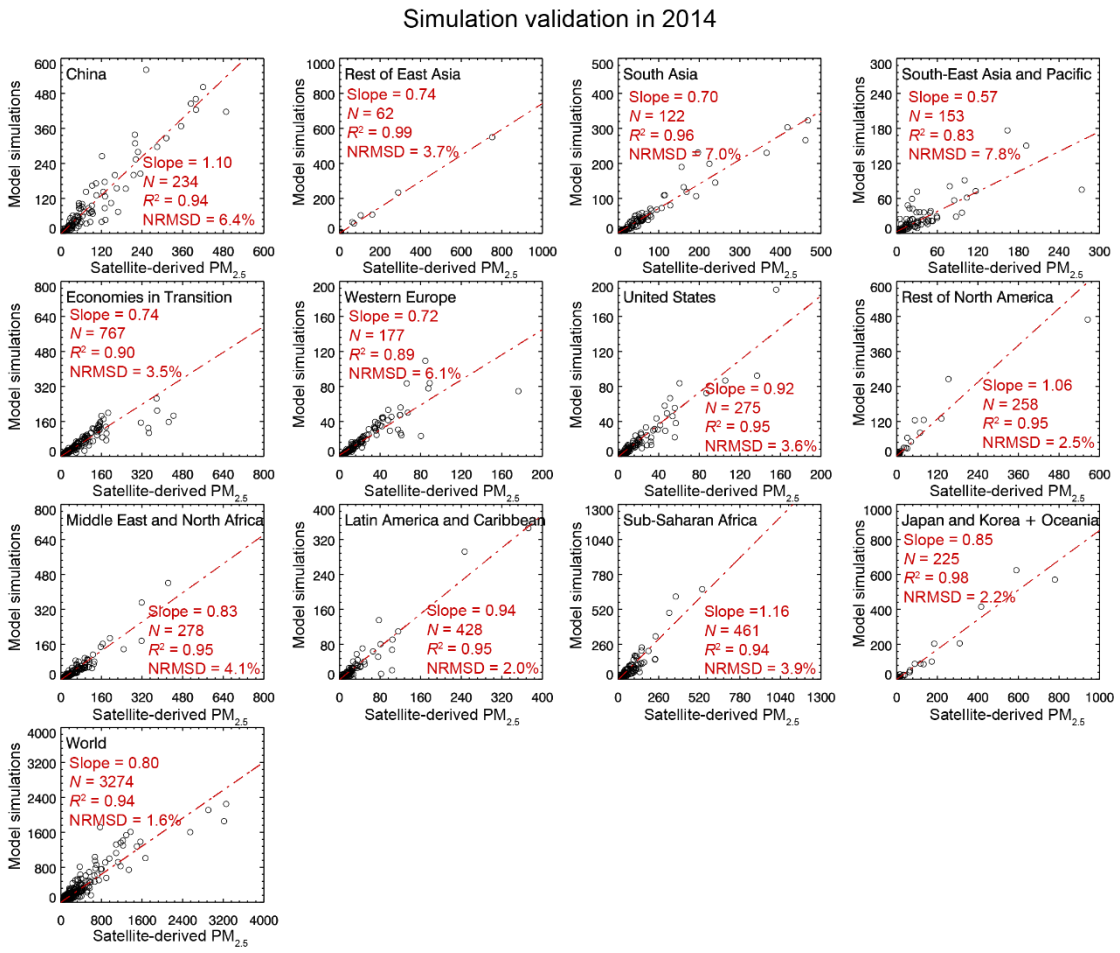


Fig. S13. Comparison between $PM_{2.5}$ simulated by the reference $PM_{2.5}$ simulated by GEOS-Chem and the satellite-derived surface $PM_{2.5}$ concentrations (μg/m³) in the year of 2014. The calculated of reference $PM_{2.5}$ is shown in Eq. 1. Each data pair represent annual mean population-weighted $PM_{2.5}$ concentrations at a model grid cell. For each grid cell of a region (e.g., China), we multiply the $PM_{2.5}$ concentration in that grid cell by the population in that grid cell, then divide by the average population (over all grid cells in that region), to focus the model evaluation over densely populated areas. Statistical analysis results are also given in each panel.

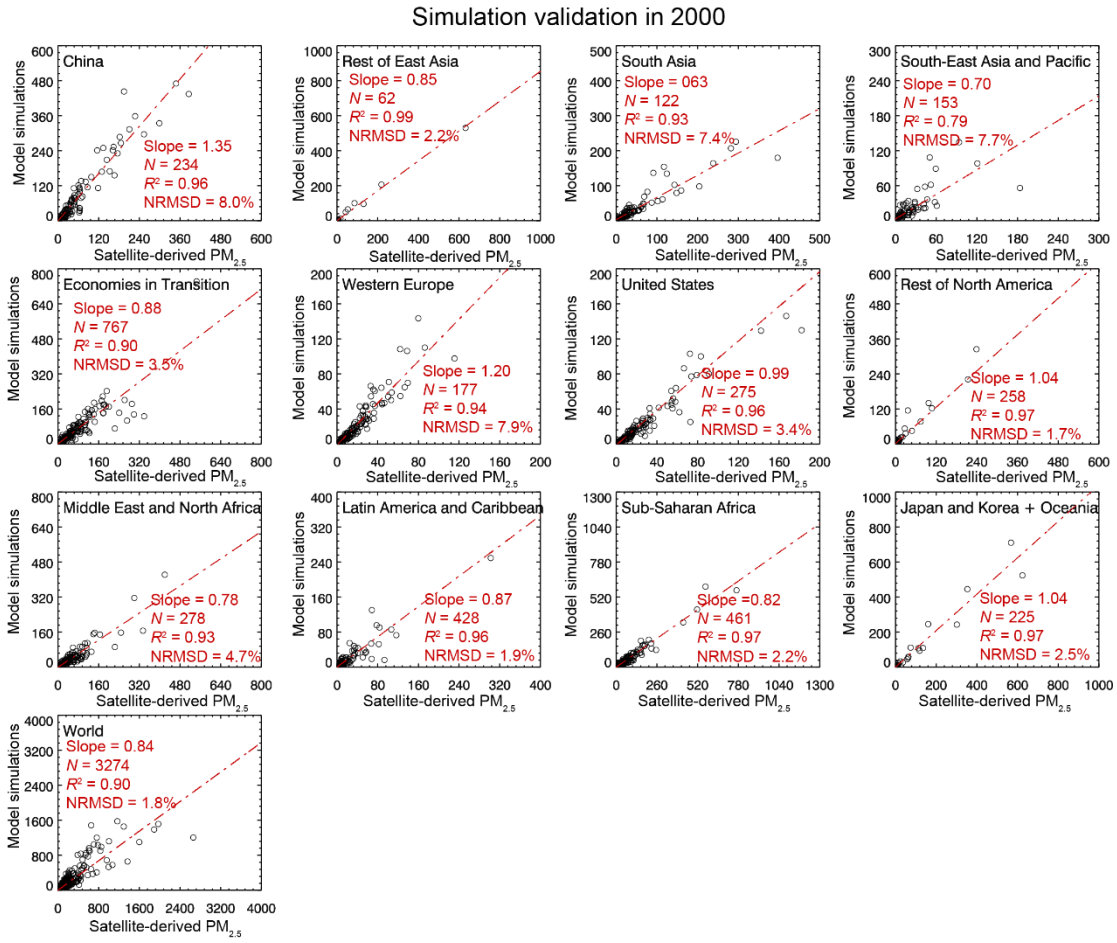


Fig. S14. Similar to Fig. S13, but for the year of 2000.

References

[1] GEOS-Chem v11-01. Available at: http://wiki.seas.harvard.edu/geos-chem/index.php/Main_Page (2017); last access: 01 Feb 2017.

[2] Lin J, Du M, Chen L, et al. Carbon and health implications of trade restrictions. Nat Commun 2019; 10: 4947.

[3] Du MX, Chen LL, Lin JT, et al. Winners and losers of the Sino-US trade war from economic and environmental perspectives. Environ Res Lett 2020; 15: 094032.

[4] Lin JT & McElroy MB. Impacts of boundary layer mixing on pollutant vertical profiles in the lower troposphere: implications to satellite remote sensing. Atmos Environ 2010; 44: 1726-39.

[5] Rienecker MM. The GEOS-5 data assimilation system: documentation of versions 5.0.1, 5.1.0, and 5.2.0. National Aeronautics and Space Administration, Goddard Space Flight Center; 2008.

[6] Wesely ML. Parameterization of surface resistances to gaseous dry deposition in regional-scale numerical-models. Atmos Environ 1989; 23: 1293-304.

[7] Wang Y, Jacob DJ & Logan JA. Global simulation of tropospheric O_3-NO_x-hydrocarbon chemistry: 1. Model formulation. J Geophys Res-Atmos 1998; 103: 10713-25.

[8] Zhang LM, Gong SL, Padro J, et al. A size-segregated particle dry deposition scheme for an atmospheric aerosol module. Atmos Environ 2001; 35: 549-60.

[9] Liu H, Jacob DJ, Bey I, et al. Constraints from 210 Pb and 7 Be on wet deposition and transport in a global three-dimensional chemical tracer model driven by assimilated meteorological fields. J Geophys Res-Atmos 2001; 106: 12109-28.

[10] Wang QQ, Jacob DJ, Spackman JR, et al. Global budget and radiative forcing of black carbon aerosol: Constraints from pole-to-pole (HIPPO) observations across the Pacific. J Geophys Res-Atmos 2014; 119: 195-206.

[11] Fountoukis C & Nenes A. ISORROPIA II: a computationally efficient thermodynamic equilibrium model for K^+-Ca^{2+}-Mg^{2+}-NH_4^+-Na^+-SO_4^{2-}-NO_3^--Cl^--H_2O aerosols. Atmos Chem Phys 2007; 7: 4639-59.

[12] Zhang L, Liu LC, Zhao YH, et al. Source attribution of particulate matter pollution over North China with the adjoint method. Environ Res Lett 2015; 10: 084011.

[13] Heald CL, Collett JL, Lee T, et al. Atmospheric ammonia and particulate inorganic nitrogen over the United States. Atmos Chem Phys 2012; 12: 10295-312.

[14] Zhang Q, Jiang X, Tong D, et al. Transboundary health impacts of transported global air pollution and international trade. Nature 2017; 543: 705-9.

[15] Pye HOT & Seinfeld JH. A global perspective on aerosol from low-volatility organic compounds. Atmos Chem Phys 2010; 10: 4377-401.

[16] Lin JT, Liu Z, Zhang Q, et al. Modeling uncertainties for tropospheric nitrogen dioxide columns affecting satellite-based inverse modeling of nitrogen oxides emissions. Atmos Chem Phys 2012; 12: 12255-75.

[17] Ni RJ, Lin JT, Yan YY, et al. Foreign and domestic contributions to springtime ozone over China. Atmos Chem Phys 2018; 18: 11447-69.

[18] Hoesly RM, Smith SJ, Feng LY, et al. Historical (1750-2014) anthropogenic emissions of reactive gases and aerosols from the Community Emissions Data System (CEDS). Geosci Model Dev 2018; 11: 369-408.

[19] Geng GN, Zhang Q, Martin RV, et al. Impact of spatial proxies on the representation of bottom-up emission inventories: A satellite-based analysis. Atmos Chem Phys 2017; 17: 4131-45.
[20] Multi-resolution Emission Inventory for China. Available at: http://www.meicmodel.org; last access: 18 Nov 2018.
[21] Li M, Liu H, Geng G, et al. Anthropogenic emission inventories in China: a review. Natl Sci Rev 2017; 4: 834-66.
[22] Zheng B, Tong D, Li M, et al. Trends in China's anthropogenic emissions since 2010 as the consequence of clean air actions. Atmos Chem Phys 2018; 18: 14095-111.
[23] Wang JX, Ni RJ, Lin JT, et al. Socioeconomic and atmospheric factors affecting aerosol radiative forcing: Production-based versus consumption-based perspective. Atmos Environ 2019; 200: 197-207.
[24] Chen Q, Fu T-M, Hu J, et al. Modelling secondary organic aerosols in China. Natl Sci Rev 2017; 4: 806-9.
[25] Fu TM, Cao JJ, Zhang XY, et al. Carbonaceous aerosols in China: top-down constraints on primary sources and estimation of secondary contribution. Atmos Chem Phys 2012; 12: 2725-46.
[26] Huang R-J, Zhang Y, Bozzetti C, et al. High secondary aerosol contribution to particulate pollution during haze events in China. Nature 2014; 514: 218-22.
[27] Ridley DA, Heald CL, Ridley KJ, et al. Causes and consequences of decreasing atmospheric organic aerosol in the United States. Proc Natl Acad Sci USA 2018; 115: 290-5.
[28] Zhang H, Yee LD, Lee BH, et al. Monoterpenes are the largest source of summertime organic aerosol in the southeastern United States. Proc Natl Acad Sci USA 2018; 115: 2038-43.
[29] Shilling JE, Zaveri RA, Fast JD, et al. Enhanced SOA formation from mixed anthropogenic and biogenic emissions during the CARES campaign. Atmos Chem Phys 2013; 13: 2091-113.
[30] Fang D, Chen B, Hubacek K, et al. Clean air for some: Unintended spillover effects of regional air pollution policies. Sci Adv 2019; 5: eaav4707.
[31] van Donkelaar A, Martin RV, Brauer M, et al. Global estimates of fine particulate matter using a combined geophysical-statistical method with information from satellites, models, and monitors. Environ Sci Technol 2016; 50: 3762-72.
[32] Burnett R, Chen H, Szyszkowicz M, et al. Global estimates of mortality associated with long-term exposure to outdoor fine particulate matter. Proc Natl Acad Sci USA 2018; 115: 9592-7.
[33] Global Burden of Disease collaborative network. Global Burden of Disease Study 2017 (GBD 2017) cause-specific mortality 1980-2017. Seattle, United States: Institute for Health Metrics and Evaluation (IHME), 2018.
[34] United Nations, Department of Economic and Social Affairs, Population Division (2019). World Population Prospects 2019, custom data acquired via website.
[35] Chafe ZA, Brauer M, Klimont Z, et al. Household cooking with solid fuels contributes to ambient $PM_{2.5}$ air pollution and the burden of disease. Environ Health Perspect 2014; 122: 1314-20.
[36] Butt EW, Turnock ST, Rigby R, et al. Global and regional trends in particulate air pollution and attributable health burden over the past 50 years. Environ Res Lett 2017; 12: 104017.

[37] Chowdhury S, Pozzer A, Dey S, et al. Changing risk factors that contribute to premature mortality from ambient air pollution between 2000 and 2015. Environ Res Lett 2020; 15: 074010.
[38] Burnett RT, Pope CA, 3rd, Ezzati M, et al. An integrated risk function for estimating the global burden of disease attributable to ambient fine particulate matter exposure. Environ Health Perspect 2014; 122: 397-403.
[39] Lelieveld J, Evans JS, Fnais M, et al. The contribution of outdoor air pollution sources to premature mortality on a global scale. Nature 2015; 525: 367-71.
[40] Forouzanfar MH, Afshin A, Alexander LT, et al. Global, regional, and national comparative risk assessment of 79 behavioural, environmental and occupational, and metabolic risks or clusters of risks, 1990-2015: a systematic analysis for the Global Burden of Disease Study 2015. Lancet 2016; 388: 1659-724.
[41] Forouzanfar MH, Alexander L, Anderson HR, et al. Global, regional, and national comparative risk assessment of 79 behavioural, environmental and occupational, and metabolic risks or clusters of risks in 188 countries, 1990-2013: a systematic analysis for the Global Burden of Disease Study 2013. Lancet 2015; 386: 2287-323.
[42] Gakidou E, Afshin A, Abajobir AA, et al. Global, regional, and national comparative risk assessment of 84 behavioural, environmental and occupational, and metabolic risks or clusters of risks, 1990-2016: a systematic analysis for the Global Burden of Disease Study 2016. Lancet 2017; 390: 1345-422.
[43] Lim SS, Vos T, Flaxman AD, et al. A comparative risk assessment of burden of disease and injury attributable to 67 risk factors and risk factor clusters in 21 regions, 1990-2010: a systematic analysis for the Global Burden of Disease Study 2010. Lancet 2012; 380: 2224-60.
[44] Stanaway JD, Afshin A, Gakidou E, et al. Global, regional, and national comparative risk assessment of 84 behavioural, environmental and occupational, and metabolic risks or clusters of risks for 195 countries and territories, 1990-2017: a systematic analysis for the Global Burden of Disease Study 2017. Lancet 2018; 392: 1923-94.
[45] Shindell D, Faluvegi G, Seltzer K, et al. Quantified, localized health benefits of accelerated carbon dioxide emissions reductions. Nat Clim Chang 2018; 8: 291-5.
[46] Anenberg SC, West JJ, Yu HB, et al. Impacts of intercontinental transport of anthropogenic fine particulate matter on human mortality. Air Qual Atmos Hlth 2014; 7: 369-79.
[47] Liang CK, West JJ, Silva RA, et al. HTAP2 multi-model estimates of premature human mortality due to intercontinental transport of air pollution and emission sectors. Atmos Chem Phys 2018; 18: 10497-520.
[48] Hoekstra R & van den Bergh JCJM. Structural decomposition analysis of physical flows in the economy. Environ Resour Econ 2002; 23: 357-78.
[49] Mi ZF, Meng J, Guan DB, et al. Pattern changes in determinants of Chinese emissions. Environ Res Lett 2017; 12: 074003.
[50] Dietzenbacher E & Los B. Structural decomposition techniques: sense and sensitivity. Econ Syst Res 1998; 10: 307-24.
[51] Mi Z, Meng J, Guan D, et al. Chinese CO_2 emission flows have reversed since the global financial crisis. Nat Commun 2017; 8: 1712.
[52] Su B & Thomson E. China's carbon emissions embodied in (normal and processing) exports and their driving forces, 2006-2012. Energy Econ 2016; 59: 414-22.

[53] Simone NW, Stettler MEJ & Barrett SRH. Rapid estimation of global civil aviation emissions with uncertainty quantification. Transport Res D-Tr E 2013; 25: 33-41.
[54] Eyring V, Kohler HW, van Aardenne J, et al. Emissions from international shipping: 1. The last 50 years. J Geophys Res-Atmos 2005; 110.
[55] Eyring V, Kohler HW, Lauer A, et al. Emissions from international shipping: 2. Impact of future technologies on scenarios until 2050. J Geophys Res-Atmos 2005; 110.
[56] Wang C, Corbett JJ & Firestone J. Improving spatial representation of global ship emissions inventories. Environ Sci Technol 2008; 42: 193-9.
[57] EMEP/CEIP 2014 Present state of emission data. Available at: https://www.ceip.at/ms/ceip_home1/ceip_home/webdab_emepdatabase/reported_emissiondata; last access: 28 Sep 2015.
[58] Giglio L, Randerson JT & van der Werf GR. Analysis of daily, monthly, and annual burned area using the fourth-generation global fire emissions database (GFED4). J Geophys Res-Biogeo 2013; 118: 317-28.
[59] Guenther AB, Jiang X, Heald CL, et al. The Model of Emissions of Gases and Aerosols from Nature version 2.1 (MEGAN2.1): an extended and updated framework for modeling biogenic emissions. Geosci Model Dev 2012; 5: 1471-92.
[60] Hudman RC, Moore NE, Mebust AK, et al. Steps towards a mechanistic model of global soil nitric oxide emissions: implementation and space based-constraints. Atmos Chem Phys 2012; 12: 7779-95.
[61] Murray LT, Jacob DJ, Logan JA, et al. Optimized regional and interannual variability of lightning in a global chemical transport model constrained by LIS/OTD satellite data. J Geophys Res-Atmos 2012; 117.
[62] Duncan Fairlie T, Jacob DJ & Park RJ. The impact of transpacific transport of mineral dust in the United States. Atmos Environ 2007; 41: 1251-66.
[63] Fairlie TD, Jacob DJ, Dibb JE, et al. Impact of mineral dust on nitrate, sulfate, and ozone in transpacific Asian pollution plumes. Atmos Chem Phys 2010; 10: 3999-4012.
[64] Zhang L, Kok JF, Henze DK, et al. Improving simulations of fine dust surface concentrations over the western United States by optimizing the particle size distribution. Geophys Res Lett 2013; 40: 3270-5.
[65] Jaeglé L, Quinn PK, Bates TS, et al. Global distribution of sea salt aerosols: new constraints from in situ and remote sensing observations. Atmos Chem Phys 2011; 11: 3137-57.
[66] United Nations publication. World Economic Situation and Prospects 2018.
[67] Crippa M, Solazzo E, Huang G, et al. High resolution temporal profiles in the Emissions Database for Global Atmospheric Research. Sci Data 2020; 7: 121.
[68] Huang T, Zhu X, Zhong Q, et al. Spatial and temporal trends in global emissions of nitrogen oxides from 1960 to 2014. Environ Sci Technol 2017; 51: 7992-8000.
[69] Huang Y, Shen H, Chen H, et al. Quantification of global primary emissions of $PM_{2.5}$, PM_{10}, and TSP from combustion and industrial process sources. Environ Sci Technol 2014; 48: 13834-43.
[70] Wang R, Tao S, Shen H, et al. Trend in global black carbon emissions from 1960 to 2007. Environ Sci Technol 2014; 48: 6780-7.
[71] Meng W, Zhong Q, Yun X, et al. Improvement of a global high-resolution ammonia emission inventory for combustion and industrial sources with new data from the residential and transportation Sectors. Environ Sci Technol 2017; 51: 2821-9.

[72] Huang Y, Shen HZ, Chen YL, et al. Global organic carbon emissions from primary sources from 1960 to 2009. Atmos Environ 2015; 122: 505-12.